

Accepted Manuscript

Computation of three-dimensional three-phase flow of carbon dioxide using a high-order WENO scheme

Magnus Aa. Gjennestad, Andrea Gruber, Karl Yngve Lervåg, Øyvind Johansen, Åsmund Ervik et al.

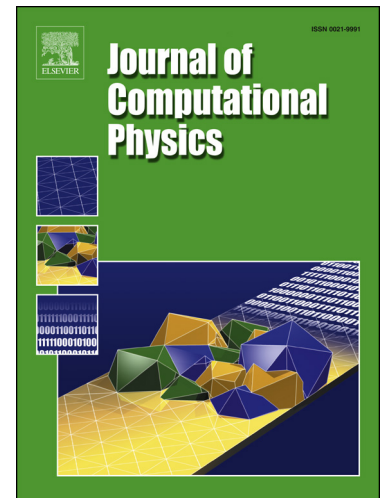
PII: S0021-9991(17)30518-1
DOI: <http://dx.doi.org/10.1016/j.jcp.2017.07.016>
Reference: YJCPH 7463

To appear in: *Journal of Computational Physics*

Received date: 23 February 2017
Revised date: 23 June 2017
Accepted date: 8 July 2017

Please cite this article in press as: M.Aa. Gjennestad et al., Computation of three-dimensional three-phase flow of carbon dioxide using a high-order WENO scheme, *J. Comput. Phys.* (2017), <http://dx.doi.org/10.1016/j.jcp.2017.07.016>

This is a PDF file of an unedited manuscript that has been accepted for publication. As a service to our customers we are providing this early version of the manuscript. The manuscript will undergo copyediting, typesetting, and review of the resulting proof before it is published in its final form. Please note that during the production process errors may be discovered which could affect the content, and all legal disclaimers that apply to the journal pertain.



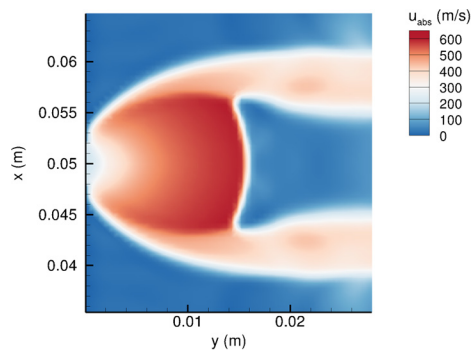
Graphical abstract

Computation of three-dimensional three-phase flow of carbon dioxide using a high-order WENO scheme

Journal of Computational Physics ●●●, ●●●, ●●●

Magnus Aa. Gjennestad, Andrea Gruber, Karl Yngve Lervåg, Øyvind Johansen, Åsmund Ervik, Morten Hammer, Svend Tollak Munkejord*

SINTEF Energy Research, P.O. Box 4761 Sluppen, NO-7465 Trondheim, Norway



Highlights

- A WENO method for single-, two- and three-phase flow of CO₂ is developed.
- The flow is described by a homogeneous equilibrium model including viscosity.
- The thermodynamic properties are calculated using the Span-Wagner equation of state.
- The method is parallelized using domain decomposition.
- Underexpanded CO₂ jets are studied and good agreement with experiments is obtained.

Computation of three-dimensional three-phase flow of carbon dioxide using a high-order WENO scheme

Magnus Aa. Gjennestad, Andrea Gruber, Karl Yngve Lervåg, Øyvind Johansen, Åsmund Ervik, Morten Hammer, Svend Tollak Munkejord*

SINTEF Energy Research, P.O. Box 4761 Sluppen, NO-7465 Trondheim, Norway

Abstract

We have developed a high-order numerical method for the 3D simulation of viscous and inviscid multiphase flow described by a homogeneous equilibrium model and a general equation of state. Here we focus on single-phase, two-phase (gas-liquid or gas-solid) and three-phase (gas-liquid-solid) flow of CO₂ whose thermodynamic properties are calculated using the Span–Wagner reference equation of state. The governing equations are spatially discretized on a uniform Cartesian grid using the finite-volume method with a fifth-order weighted essentially non-oscillatory (WENO) scheme and the robust first-order centred (FORCE) flux. The solution is integrated in time using a third-order strong-stability-preserving Runge–Kutta method. We demonstrate close to fifth-order convergence for advection-diffusion and for smooth single- and two-phase flows. Quantitative agreement with experimental data is obtained for a direct numerical simulation of an air jet flowing from a rectangular nozzle. Quantitative agreement is also obtained for the shape and dimensions of the barrel shock in two highly underexpanded CO₂ jets.

Keywords: CO₂, decompression, underexpanded jet, Mach disk, shock capturing, WENO

1. Introduction

The deployment of CO₂ capture and storage (CCS) is regarded as a key strategy to mitigate global warming [1]. To design and operate CCS systems in a safe and cost-effective way, accurate data and models are needed [2]. This includes models and methods to simulate the near field of a CO₂ jet resulting from the decompression of equipment containing high-pressure CO₂. The data from these near-field simulations are e.g. used as input for less resolved simulations of the dispersion of CO₂ in the terrain [3–5].

This type of scenario puts some requirements on the models and numerical methods to be used. Depressurization of CO₂ from supercritical pressures typically involves complex three-phase (gas-liquid-solid) flow. Describing this kind

*Corresponding author.

Email address: [svend.t.munkejord \[a\] sintef.no](mailto:svend.t.munkejord@sintef.no) (Svend Tollak Munkejord)

26 of flow necessitates a multiphase flow model and an equation of state (EOS) that is accurate and capable of capturing
27 the three-phase behaviour [6, 7]. For high vessel pressures, the CO₂ jet resulting from a leak will form a shock, which
28 the numerical method must be able to capture. In addition, we would like the numerical method to maintain discrete
29 conservation of mass, momentum and energy and, due to computational efficiency, to be of high order in smooth
30 regions of the computational domain, without producing spurious oscillations in the solution near discontinuities.

31 Wareing *et al.* [7, 8] and Woolley *et al.* [9] studied CO₂ jets using a Reynolds-averaged Navier–Stokes model. The
32 flow model was combined with a composite EOS [7] to describe three-phase CO₂ flow. The flow model was solved
33 using a conservative, shock-capturing second-order scheme, as described by Falle [10].

34 However, advances have been made in constructing and implementing finite-volume, shock capturing and conser-
35 vative numerical methods of higher order. Titarev and Toro [11] presented a procedure relying on weighted essentially
36 non-oscillatory (WENO) interpolation [12] and achieved fifth-order convergence for their smooth and inviscid two-
37 dimensional isentropic vortex problem. Their scheme was extended to include interpolation of velocity derivatives and
38 computation of viscous transport of momentum and dissipation of kinetic energy by Coralic and Colonius [13]. Such a
39 numerical scheme is suitable for execution on parallel computers by domain decomposition [14].

40 In research on numerical methods for compressible multiphase flow, the ideal-gas and stiffened-gas EOS [15, 16]
41 are commonly employed, due to their simplicity and relatively large number of applications. This is true both for 1D
42 [17–19] and 3D models [e.g. 13]. The stiffened-gas EOS can be regarded as a linearization about a reference state.
43 In many cases, however, it is necessary to consider more adapted EOSs in order to achieve the necessary accuracy.
44 This often entails a significantly higher computational complexity. As an example, Dumbser *et al.* [20] presented an
45 unstructured WENO scheme employing a real EOS for water.

46 For CCS applications, it is often necessary to describe a large thermodynamic property space, involving multiple
47 phases, for instance for the depressurization from a transport pipeline operated at a supercritical pressure around 100 bar
48 down to atmospheric conditions. In these cases, an accurate EOS is required [6], such as the one by Span and Wagner
49 [21] (SW). Therefore, in order to perform high-fidelity near-field studies of CO₂ jets, we need to combine a high-order
50 numerical scheme with a general EOS.

51 This combination would also benefit the development of predictive fluid-structure models aiding in the design of
52 CO₂-transport pipelines against running fractures [22, 23]. For practical and computational reasons, the CO₂ flow is
53 commonly described using a 1D model, which implies a simplified description of the pressure forces on the opening
54 pipe flanks [22]. A full 3D description of the flow might provide more accurate predictions.

55 In the present work we want to study complex CO₂ flows which may be single phase, two-phase (gas-liquid or
56 gas-solid) or three-phase (gas-liquid-solid). In doing so, we extend the high-order scheme of Titarev and Toro [11]
57 and Coralic and Colonius [13], applying it to the homogeneous equilibrium multiphase flow model and a formulation
58 allowing the use of a general EOS. Since the applications we are interested in typically involve sharp temperature
59 gradients, we include heat conduction in our model and in the numerical treatment of diffusive fluxes, as well as a
60 temperature-dependent viscosity.

61 We validate the implementation of the model and numerical methods through several test cases, including a turbulent
 62 air jet from a rectangular nozzle. We also demonstrate that the numerical methods exhibit high-order convergence when
 63 dealing with diffusive fluxes and two-phase flows. Finally, we perform detailed simulations of CO₂ jets, employing the
 64 SW EOS.

65 The rest of this paper is organized as follows. Section 2 reviews the governing equations, while the treatment of
 66 inflow and open boundary conditions is briefly described in Section 3. Section 4 deals with the numerical methods.
 67 Section 5 demonstrates the accuracy and robustness of the scheme, including the direct numerical simulation of an air
 68 jet, while Section 6 discusses the simulation of a CO₂ jet. Section 7 concludes the study.

69 2. Models

70 2.1. Fluid dynamics

71 We consider a three-dimensional flow of a fluid that may consist of multiple phases. The different phases are
 72 assumed to be in local equilibrium and to move with the same velocity. The flow may then be described by a
 73 homogenous equilibrium model (HEM), which can be formulated as a system of balance equations,

$$\partial_t \mathbf{Q} + \partial_x \mathbf{F} + \partial_y \mathbf{G} + \partial_z \mathbf{H} = \mathbf{S}(\mathbf{Q}). \quad (1)$$

74 Here \mathbf{F} , \mathbf{G} and \mathbf{H} are the fluxes in the x -, y - and z -direction, respectively, and $\mathbf{S}(\mathbf{Q})$ is the vector of source terms. The
 75 vector \mathbf{Q} contains the state variables,

$$\mathbf{Q} = [\rho, \rho u_x, \rho u_y, \rho u_z, E]^T, \quad (2)$$

76 where ρ is the fluid density, u_x , u_y and u_z are the flow velocities and E is the total energy density. Thus the system (1)
 77 describes conservation of mass and balance of momentum and energy of the fluid. The total energy is

$$E = \rho e + \frac{1}{2} \rho (u_x^2 + u_y^2 + u_z^2), \quad (3)$$

78 where e is the specific internal energy of the fluid. The total energy is thus the sum of internal and kinetic energy.

79 The fluxes are

$$\mathbf{F} = \begin{bmatrix} \rho u_x \\ \rho u_x^2 + p - \sigma_{xx} \\ \rho u_y u_x - \sigma_{xy} \\ \rho u_z u_x - \sigma_{xz} \\ (E + p)u_x - u_i \sigma_{xi} - \kappa \partial_x T \end{bmatrix}, \quad (4)$$

$$\mathbf{G} = \begin{bmatrix} \rho u_y \\ \rho u_x u_y - \sigma_{yx} \\ \rho u_y^2 + p - \sigma_{yy} \\ \rho u_z u_y - \sigma_{yz} \\ (E + p)u_y - u_i \sigma_{yi} - \kappa \partial_y T \end{bmatrix}, \quad (5)$$

81 and

$$\mathbf{H} = \begin{bmatrix} \rho u_z \\ \rho u_x u_z - \sigma_{zx} \\ \rho u_y u_z - \sigma_{zy} \\ \rho u_z^2 + p - \sigma_{zz} \\ (E + p)u_z - u_i \sigma_{zi} - \kappa \partial_z T \end{bmatrix}. \quad (6)$$

82 Herein, p is the fluid pressure, T is the temperature, κ is the thermal conductivity and σ_{ij} is the viscous stress tensor.
83 With these fluxes, and no source terms, (1) corresponds to the Euler equations with added diffusive fluxes for viscous
84 transport of momentum and conductive transport of heat.

85 We assume zero bulk viscosity, in which case the viscous stress tensor is given by the velocity derivatives and the
86 dynamic viscosity η as [24]

$$\sigma_{ij} = \eta \left(\partial_i u_j + \partial_j u_i - \frac{2}{3} \delta_{ij} \partial_k u_k \right). \quad (7)$$

87 2.2. Thermophysical properties

88 In order to close the system (1), we must employ a thermodynamic equation of state (EOS). We assume local
89 thermodynamic phase equilibrium and consider only pure components. In this paper, we make use of the ideal gas EOS
90 (IG), the Peng–Robinson [25] EOS (PR) and the multi-parameter Span–Wagner [21] reference EOS (SW) for CO₂.
91 Both PR and SW describe gas-liquid systems. By coupling SW to an additional model for the solid CO₂ phase, it can
92 be extended to systems including a solid phase and be used to describe solid formation, as described in Hammer *et al.*
93 [6].

94 The thermal conductivity κ is assumed constant throughout this work. The dynamic viscosity η , however, has
95 a strong temperature dependence and cannot always be assumed constant. Therefore, we use the TRAPP extended
96 corresponding state model due to Ely and Hanley [26] for the dynamic viscosity in cases with large temperature
97 variations.

98 3. Boundary conditions

99 3.1. Nozzle inflow

100 For the CO₂ jet to be studied, we model inflow through a nozzle located at the domain boundary. Boundary
101 conditions in the nozzle region are set by the isentropic steady-state Bernoulli equations,

$$dh + u du = 0, \quad (8)$$

$$ds = 0, \quad (9)$$

102 for the specific enthalpy h , specific entropy s and velocity u of the fluid. Integrating these to the boundary from some
 103 known rest state behind the nozzle, specified e.g. by T_∞ and p_∞ , we get

$$s_\infty = s_b, \quad (10)$$

$$h_\infty = h(s_b, p_b) + \frac{1}{2}u_b^2, \quad (11)$$

104 where the boundary values have a subscript b. By setting u_b equal to the speed of sound and solving the integrated
 105 Bernoulli equations for p_b , we obtain the choke pressure at the nozzle. This procedure thus gives the pressure, entropy
 106 and flow velocity at the boundary and the boundary condition is completely specified.

107 3.2. Non-reflecting boundaries

108 Many practical flows of interest are located in physical domains that are unbounded in one or more spatial directions
 109 and require the specification of an artificial boundary in order to make the computational domain finite. The artificial
 110 boundary represents a connection between the computational domain and the surrounding far field. Care must be taken
 111 in the definition of this *open boundary*. Under-specification or over-specification of physical boundary conditions
 112 would lead to an ill-posed problem and are a classical cause of numerical instability. In fluid flows, information about
 113 the flow conditions is transmitted across the open boundaries by physical waves. These open boundaries should allow
 114 waves (especially pressure waves or acoustic waves) to travel freely in and out of the computational domain. However,
 115 the knowledge about the exterior can often be unsure or absent and additional modelling or qualified guesses about
 116 these flow conditions may be necessary. In particular, the amplitudes of the outgoing waves may be used as a starting
 117 point for the modelling of the incoming ones. This approach, named Navier–Stokes Characteristic Boundary Conditions
 118 (NSCBC), is utilized in the present work to specify the open boundaries of the computational domain, as described in
 119 the landmark paper by Poinso and Lele [27] and later refined by Sutherland and Kennedy [28] for the general context
 120 of single-phase, multi-component and reactive flows.

121 4. Numerical methods

122 The fluid-dynamical model is integrated in time using the finite-volume method on a uniform Cartesian grid. This
 123 method transforms the coupled system of PDEs (1) into a system of coupled ODEs that can be integrated in time with
 124 an appropriate Runge–Kutta method.

125 4.1. Spatial discretization

126 The semi-discrete form of the PDE system (1) is obtained by integrating it over the volume of a cell i, j, k and
 127 applying the divergence theorem,

$$\frac{d}{dt} \mathbf{Q}_{i,j,k} = \frac{1}{\Delta x} (\mathbf{F}_{i-1/2,j,k} - \mathbf{F}_{i+1/2,j,k}) + \frac{1}{\Delta y} (\mathbf{G}_{i,j-1/2,k} - \mathbf{G}_{i,j+1/2,k}) + \frac{1}{\Delta z} (\mathbf{H}_{i,j,k-1/2} - \mathbf{H}_{i,j,k+1/2}). \quad (12)$$

128 Herein, we have defined the volume-averaged state variables for the cell i, j, k ,

$$\mathbf{Q}_{i,j,k} \equiv \frac{1}{\Delta x \Delta y \Delta z} \int_{x_{i-1/2}}^{x_{i+1/2}} \int_{y_{j-1/2}}^{y_{j+1/2}} \int_{z_{k-1/2}}^{z_{k+1/2}} \mathbf{Q}(x, y, z, t) \, dx \, dy \, dz, \quad (13)$$

129 and the area-averaged fluxes over the cell edges,

$$\mathbf{F}_{i-1/2,j,k} \equiv \frac{1}{\Delta y \Delta z} \int_{y_{j-1/2}}^{y_{j+1/2}} \int_{z_{k-1/2}}^{z_{k+1/2}} \mathbf{F}(x_{i-1/2}, y, z, t) \, dy \, dz, \quad (14)$$

$$\mathbf{G}_{i,j-1/2,k} \equiv \frac{1}{\Delta x \Delta z} \int_{x_{i-1/2}}^{x_{i+1/2}} \int_{z_{k-1/2}}^{z_{k+1/2}} \mathbf{G}(x, y_{j-1/2}, z, t) \, dx \, dz, \quad (15)$$

$$\mathbf{H}_{i,j,k-1/2} \equiv \frac{1}{\Delta x \Delta y} \int_{x_{i-1/2}}^{x_{i+1/2}} \int_{y_{j-1/2}}^{y_{j+1/2}} \mathbf{H}(x, y, z_{k-1/2}, t) \, dx \, dy. \quad (16)$$

130 Approximating the flux integrals (14)-(16) using one quadrature point per cell edge, one may derive numerical
 131 schemes that are at most second-order. If one instead evaluates the flux integrals using multiple quadrature points on
 132 each cell edge, numerical methods of higher order can be constructed. The evaluation of the flux integrals is then
 133 done by first computing the numerical flux at each quadrature point, and then taking some linear combination of the
 134 computed fluxes. This procedure requires reconstruction of the fluid state and derivatives of velocity and temperature
 135 to both sides of the cell edges at each quadrature point. It also requires high-order numerical volume integration when
 136 calculating the volume-averaged primitive variables $\mathbf{V}_{i,j,k}$ from the state variables \mathbf{Q} , as noted by Coralic and Colonius
 137 [13]. That is, the integral

$$\mathbf{V}_{i,j,k} \equiv \frac{1}{\Delta x \Delta y \Delta z} \int_{x_{i-1/2}}^{x_{i+1/2}} \int_{y_{j-1/2}}^{y_{j+1/2}} \int_{z_{k-1/2}}^{z_{k+1/2}} \mathbf{V}(\mathbf{Q}(x, y, z, t)) \, dx \, dy \, dz, \quad (17)$$

138 must be approximated numerically using multiple quadrature points per cell volume and thus the state variables must
 139 be reconstructed to these quadrature points.

140 Titarev and Toro [11] presented a procedure as outlined above using WENO interpolation for reconstruction of
 141 the fluid states. This was extended to include reconstruction of derivatives and computation of diffusive fluxes by
 142 Coralic and Colonius [13]. We will rely on their methods in this work and the reader is referred to their works for a
 143 more thorough exposition. We shall here employ a fifth-order WENO scheme for reconstruction of fluid states and use
 144 fourth-order Gaussian quadrature rules, two quadrature points for each cell edge integral and four quadrature points for
 145 each cell volume integral, in all 2D simulations. In 3D, we shall use four quadrature points for each cell edge integral
 146 and eight quadratures point for each cell volume integral. As basic advective numerical flux, we employ the robust
 147 first-order centred (FORCE) scheme [29]. Regarding the calculation of the WENO weights, we employ the relations
 148 presented in [11].

149 4.1.1. Reconstructed variables

150 In order for the fluid states at the quadrature points to be consistent with the EOS, one must choose a set of
 151 five variables¹, interpolate these to the quadrature points and then use the interpolated values, the EOS and the

¹Five variables for 3D simulations, four for 2D and three for 1D.

152 thermophysical property models to compute the remaining variables needed to compute the fluxes. As noted by e.g.
153 Coralic and Colonius [13], the fluid state may be reconstructed using many different sets of variables, i.e. the choice of
154 reconstruction variables is not unique. To avoid spurious oscillations, however, it will often be necessary to reconstruct
155 in another set of variables than the state variables \mathbf{Q} [30, Sec. 14.4.3]

156 Hammer *et al.* [6] performed reconstruction in flow velocity, density and internal energy when performing 1D
157 simulations with second-order MUSCL reconstruction and the Span–Wagner reference EOS for CO₂. For simulations
158 with high-order WENO reconstruction and the ideal gas or stiffened-gas EOS, Titarev and Toro [11] and Coralic and
159 Colonius [13] performed reconstruction in the local characteristic variables. Coralic and Colonius [13] obtained the
160 local characteristic variables by multiplying the vector of primitive variables with a locally frozen transformation
161 matrix. We will follow their procedure when using the ideal-gas EOS. However, for more advanced EOSs, we use a
162 more general procedure which is described in Appendix A.

163 4.2. Temporal integration

164 For time integration, we use the three-step third-order strong-stability-preserving Runge–Kutta (RK) method [see
165 e.g. 31]. Our time steps are limited by a Courant–Friedrichs–Lewy (CFL) criterion for all cases. This is done in a
166 similar way as in [11]. For cases with viscosity and thermal conductivity, one must in addition consider the time step
167 restriction imposed by the diffusive fluxes [13]. Given a set of fluid parameters, the latter restriction will be limiting
168 for the time step length if fine enough grids are used. In practice, however, we found that the the CFL criterion was
169 sufficient to ensure stability for the grids and fluids considered in this study.

170 4.3. Phase equilibrium

171 When the balance equations (1) are advanced in time, the mass of each component, and the momentum and total
172 energy of the mixture are updated in every control volume. This allows the determination of the specific volume v and
173 internal energy e . For given e and v , the equilibrium phase distribution and the intensive variables temperature T and
174 pressure p must be determined. This calculation is called a *flash*, or more specifically an ev -flash. Mathematically,
175 the ev -flash represents a global maximization of entropy in the temperature-pressure-phase-fraction space, subject to
176 constraints on mass and internal energy. A challenging part of this calculation is to determine which phases are present.
177 Under the assumption of full equilibrium (mechanical, thermal and chemical), the phases present must have the same
178 pressure, temperature and chemical potential. For our numerical methods, we guess which phases are present and
179 then solve to meet the constrains. During this iterative procedure, all phases present are in full equilibrium. When the
180 constraints are satisfied for the trial set of phases, it must be determined if the solution is a local or a global solution by
181 introducing or removing phases. The phase distribution maximizing the entropy is the ev -flash solution.

182 At different steps in the model integration, it becomes necessary to solve different flash problems. These are still
183 global optimization problems, but they have constraints other than mass and internal energy. Depending on what
184 information is available at a given step, we solve one of the following problems to obtain the equilibrium state.

- 185 • Equilibrium calculation with specified internal energy e_{spec} and specific volume v_{spec} (*ev*-flash)
- 186 • Equilibrium calculation with specified entropy s_{spec} and specific volume v_{spec} (*sv*-flash)
- 187 • Equilibrium calculation with specified entropy s_{spec} and pressure p_{spec} (*ps*-flash)

188 When performing reconstruction in internal energy, density and velocity, we have a known internal energy e_{spec} and
189 specific volume v_{spec} . To determine the temperature, pressure and phase distribution, an *ev*-flash must be solved.

190 To set boundary-condition states from the nozzle inflow model (see Section 3.1), we must calculate the equilibrium
191 state with specified pressure p_{spec} and entropy s_{spec} . To determine the temperature and the phase fractions, the *ps*-flash
192 must be solved.

193 Giljarhus *et al.* [32] considered these equilibrium problems for single-phase gas and liquid, and two-phase gas-liquid.
194 The extension of the solution procedures to account for dry-ice along the sublimation line is described thoroughly
195 by Hammer *et al.* [6], for both the *ev*-flash and the *ps*-flash. The *sv*-flash has not been considered earlier and will
196 be treated in more detail below. We do not rely on tabulated values in the numerical procedures, but solve the EOS
197 directly.

198 4.3.1. The *sv*-flash

199 When computing the equilibrium fluid states from the set of variables \mathbf{R} available when reconstructing in the local
200 characteristic variables (see AppendixA), we must perform an equilibrium calculation with specified entropy s_{spec} and
201 specific volume v_{spec} . The whole procedure is analogous to that with specified e_{spec} and v_{spec} .

202 In principle, the EOSs we consider here can be expressed in terms of the specific Helmholtz free energy as a
203 function of temperature and density, $a(T, \rho)$. All other thermodynamic properties can be written in terms of a and its
204 derivatives. Thus, in the gas-liquid case, solving the equation set

$$\varphi(\rho_g, \rho_\ell) = \begin{bmatrix} \mu(T, \rho_g) - \mu(T, \rho_\ell) \\ p(T, \rho_g) - p(T, \rho_\ell) \end{bmatrix} = \mathbf{0}, \quad (18)$$

205 yields ρ_g^{sat} and ρ_ℓ^{sat} for a given T . μ denotes the chemical potential. Here and in the following, φ is a general set of
206 thermodynamic relations which form the left-hand side of an equation set to be solved. With the phase densities as
207 functions of temperature, the entropy and specific volume constraints can be solved for in an outer loop,

$$\varphi(T, \beta_g) = \begin{bmatrix} (v(T, \beta_g) - v_{\text{spec}}) \\ (s(T, \beta_g) - s_{\text{spec}}) \end{bmatrix} = \mathbf{0}, \quad (19)$$

208 to get the equilibrium temperature and the gas mass fraction β_g . It is also possible to solve (18) and (19) simultaneously,
209 but solving them in an nested-loop approach improves the robustness. The gas-solid equilibrium case is solved in a
210 similar manner as the gas-liquid case.

211 In the case where the equilibrium state is single-phase, the EOS provides the relation $p = p(T, 1/v_{\text{spec}})$ and we
212 solve

$$\varphi(T) = (s(T) - s_{\text{spec}}) = 0, \quad (20)$$

213 to obtain the equilibrium temperature.

214 In the gas-liquid-solid equilibrium case, i.e. the triple point, we solve

$$\varphi(\beta_g, \beta_\ell, \beta_s) = \begin{bmatrix} v_g^{\text{tr}}\beta_g + v_\ell^{\text{tr}}\beta_\ell + v_s^{\text{tr}}\beta_s - v_{\text{spec}} \\ s_g^{\text{tr}}\beta_g + s_\ell^{\text{tr}}\beta_\ell + s_s^{\text{tr}}\beta_s - s_{\text{spec}} \\ \beta_g + \beta_\ell + \beta_s - 1 \end{bmatrix} = \mathbf{0}, \quad (21)$$

215 to obtain the phase mass fractions β_g, β_ℓ and β_s . Properties with superscript tr are evaluated for the triple-point pressure
216 and temperature.

217 4.4. Speed of sound

218 The speed of sound c for a single-phase fluid is computed as

$$c = \sqrt{\left(\frac{\partial p}{\partial \rho}\right)_s}. \quad (22)$$

219 For a gas-liquid mixture in equilibrium, the mixture speed of sound can be calculated from the combined sv -flash
220 condition (19), and the modified saturation line condition (18), resulting in the following system of equations:

$$\varphi(T, p, \beta_g, \rho_g, \rho_\ell) = \begin{bmatrix} \mu(T, \rho_g) - \mu(T, \rho_\ell) \\ p - p(T, \rho_g) \\ p - p(T, \rho_\ell) \\ v(T, \beta_g, \rho_g, \rho_\ell) - v_{\text{spec}} \\ s(T, \beta_g, \rho_g, \rho_\ell) - s_{\text{spec}} \end{bmatrix} = \mathbf{0}. \quad (23)$$

221 The solution $\chi = [T, p, \beta_g, \rho_g, \rho_\ell]^T$ to (23) gives a relation for v_{spec} and s_{spec} :

$$\varphi(\chi(v_{\text{spec}}, s_{\text{spec}}), v_{\text{spec}}, s_{\text{spec}}) = \mathbf{0}. \quad (24)$$

222 Differentiating with respect to v_{spec} , we obtain

$$\partial_\chi \varphi \partial_{v_{\text{spec}}} \chi + \partial_{v_{\text{spec}}} \varphi = \mathbf{0}, \quad (25)$$

223 whose solution $\partial_{v_{\text{spec}}} \chi$ gives an isentropic $\partial_{v_{\text{spec}}} p$, that can readily be used to calculate the mixture speed of sound. A
224 similar approach is used to calculate the speed of sound for a gas-solid mixture. For coexistence of solid, gas and liquid,
225 the equilibrium model predicts that the speed of sound is zero, since the density can change isentropically without a
226 change in pressure [33, Sec. 2.8.1]. Hence, at the triple point, the HEM loses hyperbolicity. Although this behaviour is
227 believed to be unphysical, it has not caused practical problems in the present simulations.

228 4.5. Parallelization

229 It is a computationally intensive task to solve any CFD problem in three dimensions. Advanced thermodynamic
 230 models, like the EOSs used here, add even more to the computational load. It is therefore necessary to run simulations
 231 in parallel on high-performance computing (HPC) machines.

232 Since we here use explicit time integration methods, the parallelization becomes relatively straightforward. In
 233 particular, we apply a blockwise domain decomposition [34] to the spatial domain, and the spatial discretization is
 234 applied to the subdomains which are distributed over the nodes of the HPC cluster using MPI for communication. Due
 235 to the width of the WENO stencils, we require three ghost cells both on the physical domain boundaries and on the
 236 internal boundaries of each subdomain. The values in the ghost cells are synchronized as necessary, e.g. before each
 237 substep in the temporal discretization.

238 The implementation of the domain decomposition is based on PETSc [14, 35]. In particular, we follow the
 239 minimally-intrusive parallelization strategy of Ervik *et al.* [36]², where awareness of the decomposed nature of the
 240 domain is hidden from the majority of the code.

241 5. Validation

242 5.1. Advection-diffusion

243 To demonstrate the high-order convergence of the numerical methods for diffusive fluxes, we first consider a smooth
 244 problem with the 2D constant-coefficient advection-diffusion equation,

$$\partial_t q + u_x \partial_x q + u_y \partial_y q = D (\partial_x \partial_x q + \partial_y \partial_y q). \quad (26)$$

245 Here q is some quantity subject to advective and diffusive transport, u_x and u_y are the advection velocities and D is
 246 the diffusion coefficient. If we take the entire x - y plane as our domain, an analytical solution to this equation is the
 247 Gaussian pulse,

$$q(x, y, t) = \frac{1}{2\pi\sigma^2(t)} \exp\left(-\frac{(x - u_x t - x_0)^2}{2\sigma^2(t)} - \frac{(y - u_y t - y_0)^2}{2\sigma^2(t)}\right). \quad (27)$$

248 Herein, x_0 and y_0 define the initial position of the Gaussian pulse and the spread of the pulse $\sigma^2(t)$ is a function of time
 249 t and initial the spread σ_0^2 at $t = 0$ s,

$$\sigma^2(t) = 2Dt + \sigma_0^2. \quad (28)$$

250 We consider the specific problem where $x_0 = y_0 = 3/8$ m, $\sigma_0 = 1/16$ m, $u_x = u_y = 1$ m/s, and $D = 5 \times 10^{-3}$ m²/s.
 251 We solve the problem inside a periodic domain $[0, 1] \times [0, 1]$ m and note that, with the specified parameters, the value
 252 of the solution at the domain boundaries will be much smaller than any numerical errors. The initial condition follows
 253 from (27) evaluated at $t = 0$ s.

²See also the example code dm/ex13f90 included with PETSc.

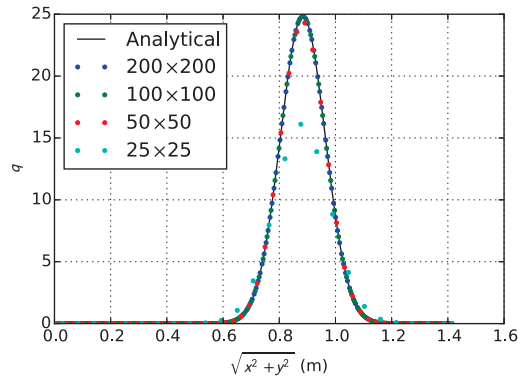


Figure 1: Comparison of the analytical solution and numerical results for the advection-diffusion problem. Values along the line $x = y$ are plotted.

Table 1: Errors and estimated convergence orders in the 2D advection-diffusion case.

Grid	L_1 -error	L_1 -order	L_∞ -error	L_∞ -order
25×25	3.208×10^{-1}	-	8.637	-
50×50	1.112×10^{-2}	4.85	4.536×10^{-1}	4.25
100×100	2.543×10^{-4}	5.45	1.060×10^{-2}	5.42
200×200	8.953×10^{-6}	4.83	3.674×10^{-4}	4.85

254 The governing equation (26) is integrated to $t = 0.25$ s. To eliminate the effect of the RK method on the convergence
 255 order, we use a constant time step of 10^{-3} s for all grid sizes. This corresponds to a CFL number of 0.2 on the 200×200
 256 grid.

257 The analytical and numerical results at $t = 0.25$ s are plotted in Figure 1. It is evident that the numerical solutions
 258 converge rapidly to the analytical solution when the grid is refined. The errors and the estimated convergence orders
 259 are presented in Table 1. The errors computed with the L_1 -norm are normalized with respect to the number of grid cells.
 260 These results show fifth-order accuracy of the numerical method, also when treating both diffusive and advective fluxes.
 261 The convergence order is better than what we should expect, since we use a fourth-order accurate quadrature rule in
 262 integrating the fluxes.

263 The results presented in this section extend the results shown by Coralic and Colonius [13]. In their paper,
 264 convergence orders are only calculated, and shown to be of fifth-order, for the isentropic vortex case in the absence of
 265 any diffusive fluxes. By applying the numerical schemes to the advection-diffusion equation, we have demonstrated
 266 fifth-order convergence also when diffusive fluxes are included.

267 5.2. Isentropic vortex

268 To validate the convergence order of the numerical schemes when applied to the fluid model with a realistic EOS, we
 269 next consider a smooth, inviscid test problem. In particular, we consider a generalization of the isentropic vortex where

270 the initial condition of the problem can be found for a general EOS. The isentropic vortex with ideal gas was studied by
 271 Balsara and Shu [37], by Titarev and Toro [11] and by Coralic and Colonius [13] to demonstrate the convergence order
 272 of their numerical schemes. In the following simulations, we first use the EOS of Peng and Robinson [25] for pure
 273 CO₂. Next, we consider the Span and Wagner [21] EOS.

To define the initial condition, we demand a uniform entropy s and prescribe a rotating velocity field,

$$u_x = u_{x,\infty} - \frac{\epsilon y}{2\pi r_0} \exp\left(\frac{1 - (r/r_0)^2}{2}\right), \quad (29)$$

$$u_y = u_{y,\infty} + \frac{\epsilon x}{2\pi r_0} \exp\left(\frac{1 - (r/r_0)^2}{2}\right). \quad (30)$$

274 Herein $u_{x,\infty}$ and $u_{y,\infty}$ are constant background velocities, ϵ is the vortex strength and r_0 is the vortex radius. We let
 275 $u_{x,\infty} = u_{y,\infty} = 0$ m/s, $\epsilon = 1000$ m/s and $r_0 = 20$ m.

276 Further, we demand that the pressure gradient give a centripetal force, whose magnitude and direction keep each
 277 fluid element moving in a circular orbit around the centre of the vortex. This results in a low-pressure region in the
 278 centre. For the ideal-gas EOS, the required pressure can be determined explicitly as a function of the radius from centre
 279 r . For a general EOS, however, we must numerically integrate the ODE

$$\frac{dp}{dr} = \frac{\rho \epsilon^2 r}{4\pi^2 r_0^2} \exp\left(1 - (r/r_0)^2\right), \quad (31)$$

280 from $r = \infty$ to $r = 0$, with initial condition $p(r = \infty) = p_\infty$, to obtain the pressure profile. The density ρ is found in
 281 each step of the integration from a ps -flash, see Section 4.3.

282 We consider two different cases,

- 283 (i) a single-phase case where the fluid is in a gaseous state everywhere, and
- 284 (ii) a two-phase case where the fluid is in a gaseous state at $r = \infty$, but condenses and enters a gas-liquid state near
 285 the centre of the vortex.

286 In the single-phase case, we let $p_\infty = 1$ MPa. The uniform entropy s is calculated at p_∞ and $T_\infty = 300$ K. With
 287 this reference state, the pressure profile obtained from (31) follows an isentrope in the phase diagram that both starts
 288 ($r = \infty$) and ends ($r = 0$) in the gas region (see the dashed line in Figure 2). Density contours are plotted Figure 3.

289 In the two-phase case, we let $p_\infty = 6$ MPa. The entropy s is taken to be the gas entropy at the saturation temperature
 290 corresponding to p_∞ . Thus we have $T_\infty = 295.1$ K. Using this reference state, we get a fluid which is in a gaseous
 291 state at $r = \infty$, but condenses and enters a gas-liquid state near the centre of the vortex due to the lower pressure. The
 292 pressure profile from (31) follows the saturation line in the phase diagram (see the dash-dotted line in Figure 2). The
 293 two-phase region is shown along with density contours in Figure 4. The solution to the isentropic vortex problem is
 294 stationary in the sense that although we have flow, the values of the state and primitive variables do not change in time.

295 It is important to note that in setting the state variables in each cell initially, we must calculate the state variables at
 296 every quadrature point in the cell and then take the average. Using only one quadrature point per cell results in a second-
 297 order error in the initial condition. The simulations were run to $t = 0.1$ s in a square domain $[-100, 100] \times [-100, 100]$ m

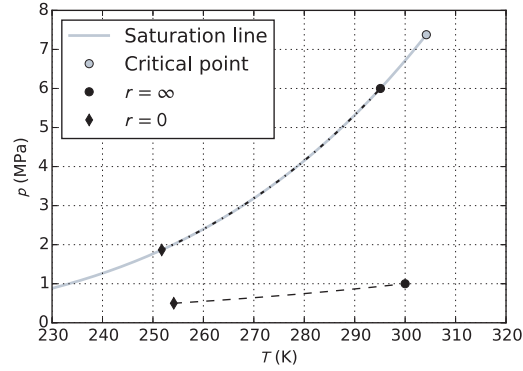


Figure 2: The pressure profiles of the isentropic vortex case, plotted in relation to the saturation pressure of CO_2 . The pressure in the single-phase case is drawn as a dashed line and the pressure in the two-phase case is drawn as a dash-dotted line.

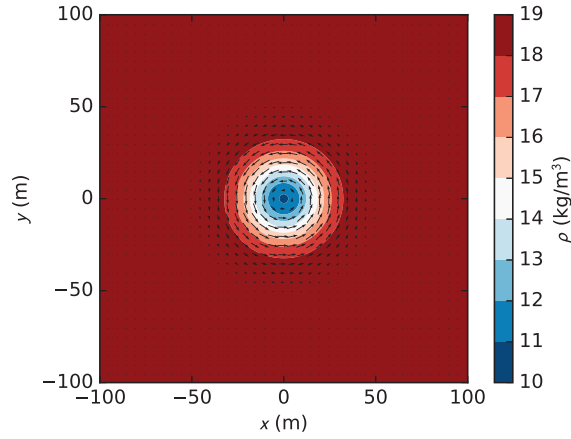


Figure 3: Density contours of the single-phase isentropic vortex case. The fluid circulates around the central low-pressure region.

298 with periodic boundary conditions and with $C_{\text{CFL}} = 0.45$. For comparison, reconstruction in both the the set $\mathbf{W} =$
 299 $[e, \rho, u_x, u_y]$ and in the local characteristic variables (see AppendixA) was performed.

300 The errors in the density field and the estimated convergence orders for the single-phase case (i) are presented in
 301 Table 2 for reconstruction in the local characteristic variables and in Table 3 for reconstruction in \mathbf{W} . It is observed that
 302 reconstruction in the characteristic variables, although much more computationally expensive, produces an error that is
 303 of the same order of magnitude as reconstruction in \mathbf{W} . The general trend is that the errors obtained with characteristic
 304 reconstruction are slightly lower. The difference is small, however, and only about 8% in the L_1 -norm on the 200×200
 305 grid. High-order convergence was obtained with both reconstruction options and significant oscillations were not
 306 observed in any simulations of this case.

307 Despite using a third-order RK method and a fourth-order quadrature rule, we get close to fifth-order convergence
 308 with both reconstruction alternatives. Similar behaviour was also observed by Titarev and Toro [11] and by Coralic

Table 2: Errors in the density field and estimated convergence orders in the single-phase isentropic vortex case (i) with the PR EOS and reconstruction in local characteristic variables.

Grid	L_1 -error	L_1 -order	L_∞ -error	L_∞ -order
25×25	1.286×10^{-2}	-	1.432×10^{-1}	-
50×50	5.975×10^{-4}	4.43	1.008×10^{-2}	3.83
100×100	2.044×10^{-5}	4.87	3.760×10^{-4}	4.74
200×200	7.410×10^{-7}	4.79	1.140×10^{-5}	5.04

Table 3: Errors in the density field and estimated convergence orders in the single-phase isentropic vortex case (i) with the PR EOS and reconstruction in $\mathbf{W} = [e, \rho, u_x, u_y]$.

Grid	L_1 -error	L_1 -order	L_∞ -error	L_∞ -order
25×25	1.314×10^{-2}	-	1.532×10^{-1}	-
50×50	6.468×10^{-4}	4.34	1.225×10^{-2}	3.64
100×100	2.196×10^{-5}	4.88	3.722×10^{-4}	5.04
200×200	8.070×10^{-7}	4.77	1.254×10^{-5}	4.89

Table 4: Errors in the density field and estimated convergence orders in the two-phase isentropic vortex case (ii) with the PR EOS and reconstruction in the local characteristic variables.

Grid	L_1 -error	L_1 -order	L_∞ -error	L_∞ -order
25×25	1.398×10^{-1}	-	1.775	-
50×50	8.523×10^{-3}	4.04	1.365×10^{-1}	3.70
100×100	3.048×10^{-4}	4.81	5.926×10^{-3}	4.53
200×200	1.119×10^{-5}	4.77	3.183×10^{-4}	4.22

Table 5: Errors in the density field and estimated convergence orders in the two-phase isentropic vortex case (ii) with the PR EOS and reconstruction in $\mathbf{W} = [e, \rho, u_x, u_y]$.

Grid	L_1 -error	L_1 -order	L_∞ -error	L_∞ -order
25×25	1.615×10^{-1}	-	1.976	-
50×50	9.200×10^{-3}	4.13	1.591×10^{-1}	3.63
100×100	3.314×10^{-4}	4.80	6.635×10^{-3}	4.58
200×200	1.215×10^{-5}	4.77	2.522×10^{-4}	4.72

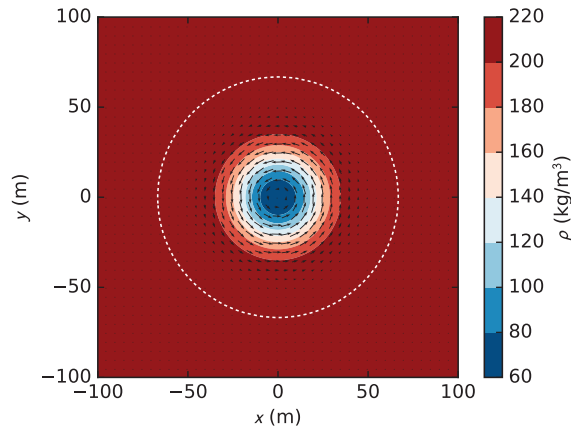


Figure 4: Density contours of the two-phase isentropic vortex case. The fluid is in a pure gas state at $r = \infty$, but condenses and enters a gas-liquid state near the centre of the vortex due to the lower pressure. The white dashed line indicates a liquid volume fraction of 10^{-12} .

and Colonius [13] and suggests that the error in the time integration method is small compared to that of the spatial discretization in this case.

We have also considered a three-dimensional, single-phase isentropic vortex problem with rotation in the x - z plane. These results also showed close to fifth-order convergence and are omitted here.

The errors in the density field and the estimated convergence orders for the two-phase case (ii) are presented in Table 4 for reconstruction in the local characteristic variables and in Table 5 for reconstruction in \mathcal{W} . Again, the general trend is that the errors are slightly smaller for reconstruction in the local characteristic variables than for reconstruction in \mathcal{W} , but again the differences are small. For this case, the difference is about 0.5% in the L_1 -norm on the 200×200 grid, while the error in the L_∞ -norm on the same grid is smaller with reconstruction in \mathcal{W} . As for the single-phase case, no significant oscillations were observed and the errors show close to fifth-order convergence.

We have also performed simulations of both case (i) and case (ii) using the more complex SW EOS, in place of the PR EOS, and reconstruction in \mathcal{W} . The errors and convergence orders are shown in Table 6 and Table 7 respectively. For both cases, the results are similar to those obtained with the PR EOS (see Table 3 and Table 5). This indicates that the order of the numerical method is not affected by the degree of complexity of the EOS underlying the phase equilibrium calculations.

To summarize, close to fifth-order convergence is observed in both the single-phase (i) and the two-phase (ii) isentropic vortex cases. This demonstrates that the high-order convergence of the numerical methods is not limited to single-phase problems with simple EOS. The results also suggest that in this case, errors in third-order temporal integration and fourth-order quadrature rules are not dominating. Differences in the error between reconstruction in \mathcal{W} and local characteristic variables are small. As reconstruction in \mathcal{W} is much less computationally intensive, it may be preferable in cases where the more advanced option is not needed in order to avoid oscillations.

Table 6: Errors in the density field and estimated convergence orders in the single-phase isentropic vortex case (i) with the SW EOS and reconstruction in $W = [e, \rho, u_x, u_y]$.

Grid	L_1 -error	L_1 -order	L_∞ -error	L_∞ -order
25×25	1.303×10^{-2}	-	1.518×10^{-1}	-
50×50	6.391×10^{-4}	4.35	1.207×10^{-2}	3.65
100×100	2.175×10^{-5}	4.88	3.663×10^{-4}	5.04
200×200	8.001×10^{-7}	4.76	1.236×10^{-5}	4.89

Table 7: Errors in the density field and estimated convergence orders in the two-phase isentropic vortex case (ii) with the SW EOS and reconstruction in $W = [e, \rho, u_x, u_y]$.

Grid	L_1 -error	L_1 -order	L_∞ -error	L_∞ -order
25×25	2.008×10^{-1}	-	2.402	-
50×50	1.150×10^{-2}	4.13	1.983×10^{-1}	3.60
100×100	4.081×10^{-4}	4.82	7.891×10^{-3}	4.65
200×200	1.467×10^{-5}	4.80	3.055×10^{-4}	4.69

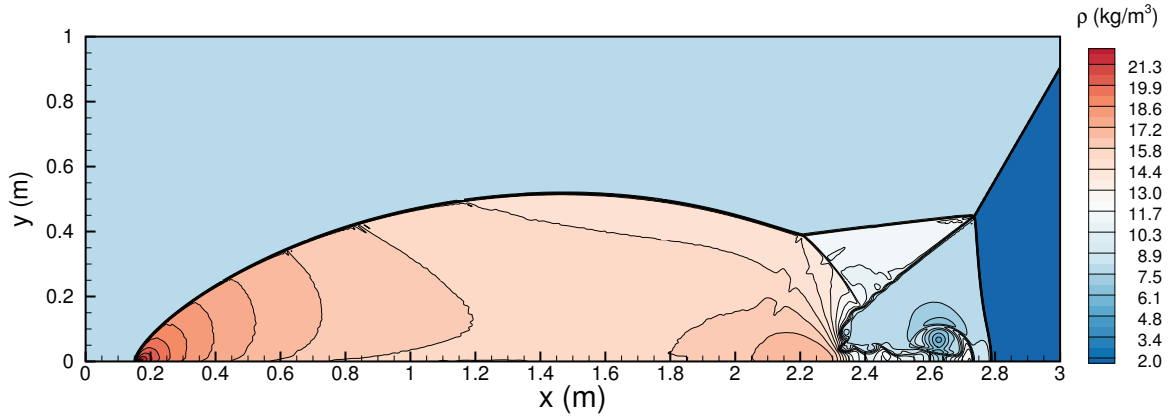
330 5.3. Double Mach reflection of strong shock

331 Next we consider a double Mach reflection of a strong shock incident on a planar wall. This problem tests the
 332 ability of the numerical methods, and their implementation, to handle strong shocks. This type of reflection problems
 333 was designed to mimic experiments where a shock propagates down a tube and hits an inserted wedge. The flow pattern
 334 resulting from the reflection of the shock on the wedge is complicated and challenging to simulate numerically. In
 335 particular, the forward jet that forms along the wall behind the first Mach stem (from approximately $x = 2.3$ m to
 336 $x = 2.8$ m in Figure 5) is difficult to resolve [38].

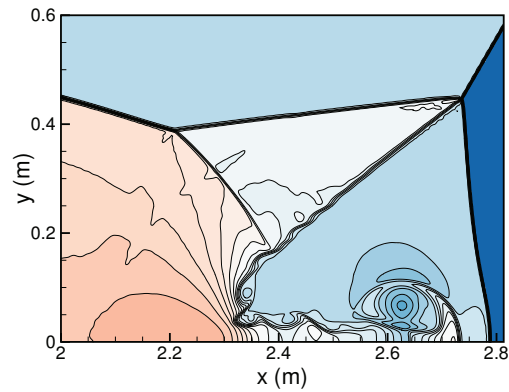
337 To have results that could be compared with those from the literature, the simulation was run with parameters that
 338 seem to be the most common, e.g. the parameters used by Titarev and Toro [11]. This also implies the ideal-gas EOS
 339 and adiabatic constant $\gamma = 1.4$.

340 We consider a domain $[0, 4] \times [0, 1]$ m. A shock is initiated with a right-moving Mach 10 front incident on the
 341 x -axis at $x = 1/6$ m and a forward angle of 60° . The undisturbed region in front of the shock is at rest with $p = 1$ Pa
 342 and $\rho = 1.4 \text{ kg/m}^3$. In post-shock region the fluid moves with velocities $u_y = -4.125 \text{ m/s}$ and $u_x = -\sqrt{3}u_y$, and has
 343 $p = 116.5 \text{ Pa}$ and $\rho = 8.0 \text{ kg/m}^3$.

344 The south wall is reflecting for $x \geq 1/6$ m and has post-shock values for $x < 1/6$ m. The eastern boundary has
 345 a zero-gradient boundary condition and the western boundary carries post shock values. The northern boundary is
 346 dynamic with post-shock values in the post-shock region and undisturbed values in the undisturbed region. For further
 347 details on the problem and how it is defined, the reader is referred to Woodward and Colella [38]. A note on the setup
 348 of the case is given by Kemm [39].



(a) Whole flow field



(b) Close-up

Figure 5: Contour plot of density in the double Mach reflection problem. Thirty contour lines in the range $[2 \text{ kg/m}^3, 22 \text{ kg/m}^3]$ are used.

349 We use a CFL number of $C_{\text{CFL}} = 0.4$ and a grid size of 1920×480 . To avoid spurious oscillations, it was necessary
 350 to perform reconstruction in the local characteristic variables for this case (see AppendixA).

351 A contour plot of the density at $t = 0.2 \text{ s}$ is shown in Figure 5. We observe that both Mach stems (starting at about
 352 $x = 0.15 \text{ m}$ and $x = 2.8 \text{ m}$) are sharp and that the details of the jet structure (in the lower part of the figure around
 353 $x = 2.5 \text{ m}$) are well-resolved. The positions of the shocks and discontinuities compare well with results from the
 354 literature [11, 12, 38, 40]. The same is true for the positions of the isodensity lines and the level of detail obtained here,
 355 compared to the fifth-order WENO reconstruction scheme on the same grid size in [11]. We conclude that the solution
 356 obtained here is in good agreement with that which is generally accepted in the literature.

357 5.4. Air jet flow from rectangular nozzle

358 The present validation test consists of a 3D direct numerical simulation of a transitional subsonic air jet issuing from a
 359 rectangular nozzle into quiescent air. The chosen configuration (with air modelled as an ideal gas) is computationally less
 360 expensive than the main demonstration case of the present paper, the supersonic CO₂ jet with complex thermodynamic
 361 behaviour (Section 6). It retains, however, some of its general flow features and, due to its straightforward boundary
 362 condition specification, can be conveniently compared with experimental data presented by Deo *et al.* [41].

363 The air jet issues with a centreline velocity of $u_{y,c,0} = 26.3$ m/s into initially quiescent air at a temperature of 293 K
 364 and pressure of 1 atm. The nozzle configuration consists of a rectangular slot of dimensions $w \times h$ characterized by
 365 high aspect ratio $w/h \sim 10$ where $h = 5.6$ mm, as in [41] resulting in a jet Reynolds number $Re_{jet} = \rho u_{y,c,0} h / \eta \sim$
 366 10^5 . Furthermore, the imposed jet inlet velocity distribution follows a “top-hat” profile to reproduce the effects
 367 of a conventional smoothly-contracting nozzle shape with laminar boundary layers, as discussed in [41]. For the
 368 experimental conditions that are targeted in the present work, the jet’s own turbulent velocity fluctuations are considered
 369 relatively unimportant and no velocity perturbations are introduced at the jet inlet. Natural perturbations of the acoustic
 370 field, intrinsically represented by the present compressible formulation, are sufficient to cause the jet flow to become
 371 unstable and break-up. The direction of the jet flow is in the positive y -direction. The two-dimensionality of the jet at
 372 the inlet nozzle is ensured by a periodic boundary condition in the spanwise direction z to eliminate border effects.
 373 Open, non-reflecting boundary conditions are imposed at the upper y boundary and at both x boundaries.

374 Figure 6 presents a visualization of the three-dimensional computational domain and a snapshot of the flow at
 375 $t = 35$ ms. The domain extends $L_y = 20$ cm in the x - and y -directions and 5 cm in the z -direction. The computational
 376 domain is discretized by $400 \times 400 \times 100$ grid nodes in the x -, y - and z -direction, respectively. This gives a constant
 377 spatial resolution of 0.5 mm throughout the computational domain and implies that the jet inlet dimension h is resolved
 378 by twelve grid nodes, while $C_{CFL} = 0.3$ in this three-dimensional simulation.

379 After the simulation is started, a settling time approximately equal to $t_{ini} \sim L_y / u_{y,c,0} = 7.6$ ms is allowed in order to
 380 ensure that the initial transient is transported outside of the computational domain. The time step is allowed to adapt
 381 to the varying CFL conditions. After the initial transient, however, it is observed that it stabilizes around $\Delta t \sim 0.4$ μ s.
 382 Sampling of the solution is started for $t > t_{ini}$, every 500 time steps or 0.2 ms (corresponding approximately to the
 383 characteristic jet time $t_{jet} = h / u_{y,c,0}$). Sampling is stopped at $t_{end} = 50$ ms after approximately 5.5 domain transit times
 384 and 238 characteristic jet times t_{jet} . Figure 7a illustrates the spatial pattern of the mean jet (wall-normal) velocity
 385 component that is averaged in time and in the homogeneous spanwise direction (z) and normalized by the centreline jet
 386 exit velocity $u_{y,c,0}$. Figure 7b analogously shows the normalized root mean square of the velocity fluctuation in the jet
 387 direction. The typical features of jet flows are present with a clearly visible potential core ($u_y \sim u_{y,c,0}$) characterized
 388 by low level of velocity fluctuations. Downstream of it, as the jet spreads, the velocity fluctuations increase due to
 389 entrainment of the surrounding air and jet break-up.

390 Figure 8 provides a more quantitative measure of the spatial extent of the potential core and of the characteristic
 391 mean velocity decay in the region of self-similarity. The length of the potential core, equal to $4h$, is in very good

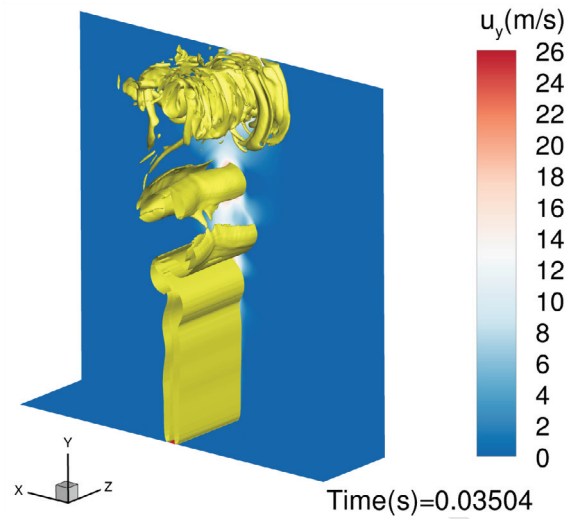
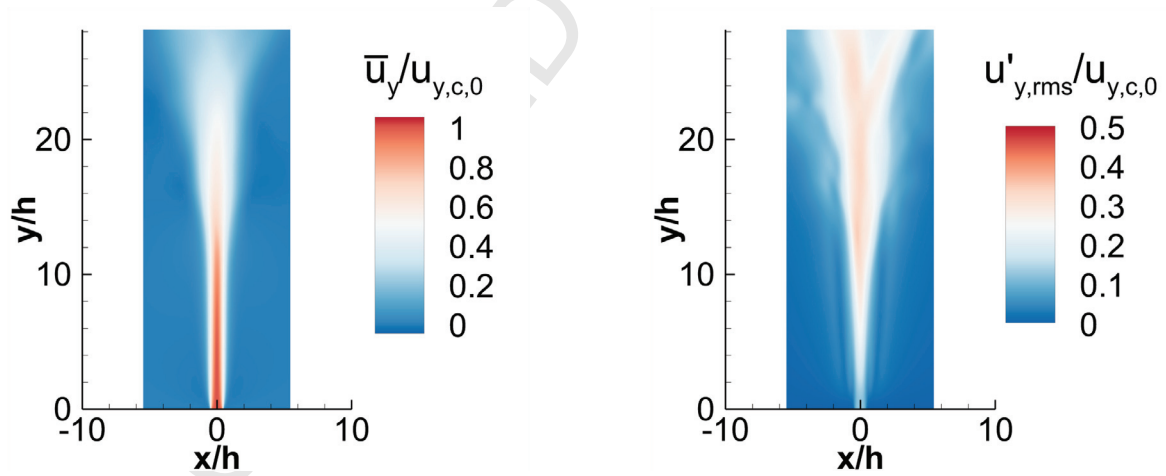


Figure 6: Air jet: Visualization of the flow and computational domain. The yellow colour indicates the 2500/s vorticity magnitude.



(a) Average of the velocity component in the jet direction, \bar{u}_y .

(b) Average of the root mean square of the velocity fluctuation $u'_{y,rms}$ in the jet direction.

Figure 7: Air jet: Pointwise temporal and spatial (in z -direction) average velocity quantities, normalized by the centreline value at the nozzle exit, $u_{y,c,0}$.

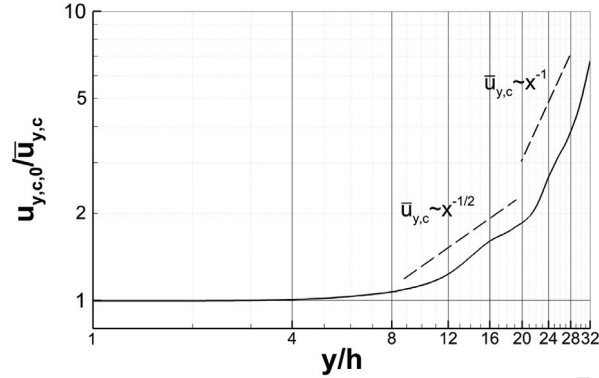


Figure 8: Air jet: 1D profile of the normalized centreline mean jet velocity $u_{y,c,0}/\bar{u}_y$ illustrating the well-known decay rates in the jet self-similar region.

392 accordance with the values reported by Deo *et al.* [41]. Furthermore, the characteristic 1/2-power law inverse decay can
 393 also be clearly observed, indicating a statistically two-dimensional behaviour of the jet, together with the appearance,
 394 further downstream, of the inversely-linear decay that indicates transition to a (more three-dimensional) axisymmetric
 395 form [41]. As pointed out in [41], the logarithmic scale used in the abscissa is essential to identify the points of
 396 transition from statistically two-dimensional to three-dimensional mean flow. Although a considerable spread in the
 397 specific spatial location of this transition is present in the available data, see Figures 6 and 7 in [41], the present results
 398 are consistent with the observed trend that the transition is delayed for increasing slot aspect ratios and anticipated
 399 for decreasing ones. The present aspect ratio w/h is approximately 10 with the transition starting 20 nozzle widths
 400 h downstream of the jet inlet, while for the aspect ratios of 30 and 60 investigated experimentally by [41], the same
 401 transition starts at 30 and 50 nozzle widths h downstream of the jet inlet. Finally, it is worth noticing the very good
 402 accordance between the present results and the results presented in Figure 7 of [41] with respect to the spatial evolution
 403 of the centreline velocity fluctuations, see Figure 9: the rapid increase for y/h between 0 and 10, the peak located
 404 between 10 and 20 and the following decay.

405 Figure 10 complements the previous analysis by providing insight into the time-dependent behaviour of the flow
 406 structure in the near field. The power spectrum (distribution of the energy of a waveform among its different frequency
 407 components) of the fluctuating instantaneous velocity is obtained through a discrete Fourier transform and plotted
 408 versus the frequency, normalized by the characteristic frequency defined as $1/t_{\text{jet}} = u_{y,c,0}/h$ for a sampling location
 409 within the potential core region (at $y/h = 3$). The presence of broad peaks in the spectrum indicates the generation of
 410 regularly-occurring large-scale coherent vortices, a well-known feature of jet flows. Furthermore, the observed decay
 411 of approximately two orders of magnitude in the spectrum is consistent with the experimental observations described
 412 in [41].

413 In summary, the method seems able to accurately capture the main features of transitional planar jets at the

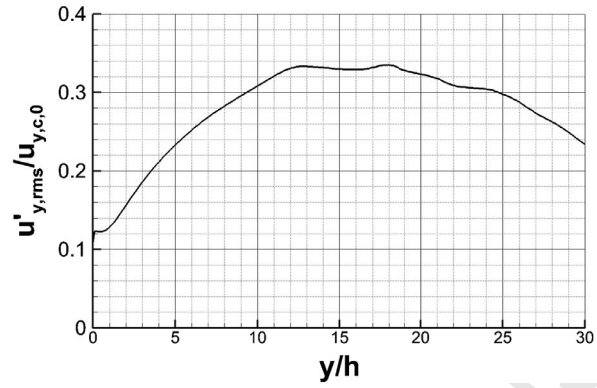


Figure 9: Air jet: 1D profile of the normalized fluctuating jet velocity $u'_{y,rms}/u_{y,c,0}$ illustrating the well-known decay rates in the jet self-similar region and peak in the turbulent fluctuations for $y/h \sim 10$.

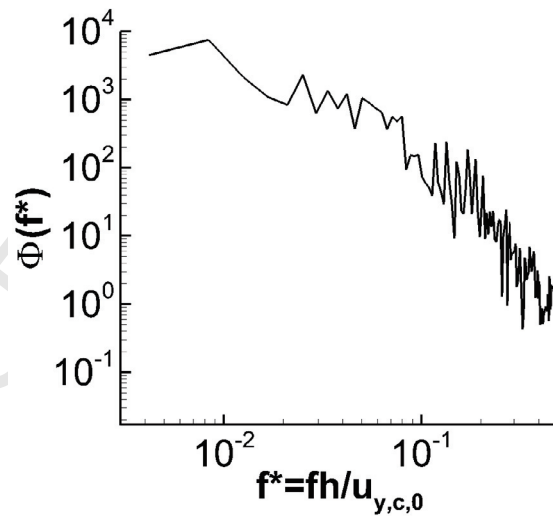


Figure 10: Air jet: Power spectrum of the instantaneous velocity sampled at $y/h = 3$ on the centreline of the jet potential core.

414 resolution employed in the present test.

415 **6. Simulation of CO₂ jet**

416 As an application of our method, we now consider two cases involving high-speed flow of CO₂, including phase
417 change and three-phase (gas-liquid-solid) flow.

418 *6.1. Case A*

419 Some relevant experimental data were presented by Li *et al.* [42], and we focus on the case labelled “RHP = 0.030”,
420 see Figure 13.

421 *6.1.1. Case description*

422 Stagnant pure CO₂ of temperature $T = 40\text{ }^\circ\text{C}$ and pressure $p = 52.2\text{ bar}$ is expanded through a round hole of
423 diameter $d_e = 1\text{ mm}$. We consider that CO₂ has replaced air in the vicinity of the jet, so the initial condition in the
424 computational domain is stagnant CO₂ of temperature $T_0 = 20\text{ }^\circ\text{C}$ and pressure $p_0 = 1\text{ bar}$. At $t = 0\text{ s}$, the CO₂ starts
425 flowing through the hole. The jet is highly underexpanded and starts forming a barrel shock, which attains a steady
426 state after about $t = 0.25\text{ ms}$. The Reynolds number at the inlet is 6×10^5 .

427 In this case, the thermodynamic properties of pure CO₂ are calculated as described in Section 2.2, with the SW
428 EOS. The thermal conductivity is set to 0.0145 W/(m K) .

429 *6.1.2. Computational set-up*

430 The computational domain, shown in Figure 11, is a cube of edge length 5 cm , divided into an equidistant grid. The
431 hole geometry is represented by a Cartesian approximation and the inflow condition is described in Section 3.1. At
432 the inlet edge, the boundary condition outside the hole is a no-slip wall. The other boundaries are governed by the
433 NSCBC (see Section 3.2) employing a far-field pressure of 1 bar and an α -coefficient of 10.0 . Here, the jet flow is in
434 the y direction.

435 Two grids were employed, with 200^3 and 400^3 cells. In the latter case, the inlet hole had eight cells across the
436 diameter. The computations were performed using the fourth-order accurate quadrature rule (see Section 4.1) with
437 the WENO scheme and $C_{\text{CFL}} = 0.333$. In the WENO scheme, the internal energy, density and velocity were used as
438 reconstruction variables, and this combination was found to work well.

439 *6.1.3. Results*

440 Pressure contours of the developing barrel shock are displayed in Figure 12, while Figure 14a shows Mach-number
441 contours at $t = 0.5\text{ ms}$. In the computation, the state is gas-liquid-solid in a small region close to the nozzle exit. The
442 gas-solid state is found in a larger region, particularly inside the barrel shock, but there is also some solid in the zone
443 beyond the barrel shock. This is illustrated in Figure 14b. In the figure, the solid mass fraction is indicated by the

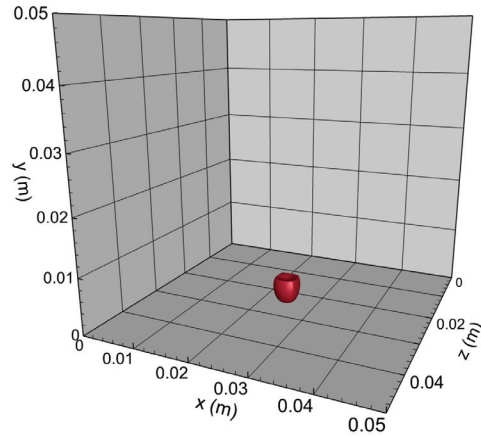


Figure 11: CO₂ jet A: Computational domain including the steady-state $Ma = 2.5$ isocontour in red. The inlet is in the middle of the x - z plane.

444 different coloured contours, while the liquid area, appearing near the inlet, is denoted by green colour, which is the
 445 1 % isocontour of the liquid mass fraction. Although quantitative measurements are not available in Li *et al.* [42], we
 446 expect the present method to underestimate the post-shock solid mass fraction in this case due to the assumption of full
 447 thermodynamic equilibrium.

448 Temperature contours are shown in Figure 14c. It can be seen that the CO₂ jet core is at about -70 °C, while the
 449 coldest temperature, about -100 °C, is appearing right before the Mach disk, due to the strong expansion.

450 In Figure 15, the Mach number and the pressure are plotted along the jet centre line. It can be seen that the position
 451 of the Mach disk is $l_{MD} = 4.8$ mm. This position can also be estimated by the correlation recommended by Franquet
 452 *et al.* [43]:

$$l_{MD} = d_c \sqrt{\frac{p/p_0}{2.4}} \approx 4.7 \text{ mm.} \quad (32)$$

453 This is in good agreement with the present result.

454 An accurate position of the Mach disk cannot be obtained from the photograph in Figure 13 or the description in Li
 455 *et al.* [42]. However, we estimate that the position of the Mach disk is roughly at half a centimetre in that photograph.
 456 Thus there is good agreement between the photograph and the present result. Further, in Figure 14a, it can be seen that
 457 the boundary layer around the jet starts widening at about 4 cm. This is also in agreement with Figure 13. However, in
 458 that photograph, one can see ice at the nozzle exit, labelled “dry ice bank”. In view of the high CO₂ exit velocity, we
 459 find it unlikely that dry-ice particles deposit immediately at the exit. The ice may well be frozen moisture from the
 460 surrounding air.

461 6.2. Case B

462 Finally, we consider the CO₂ jet presented as Test B in Pursell [44].

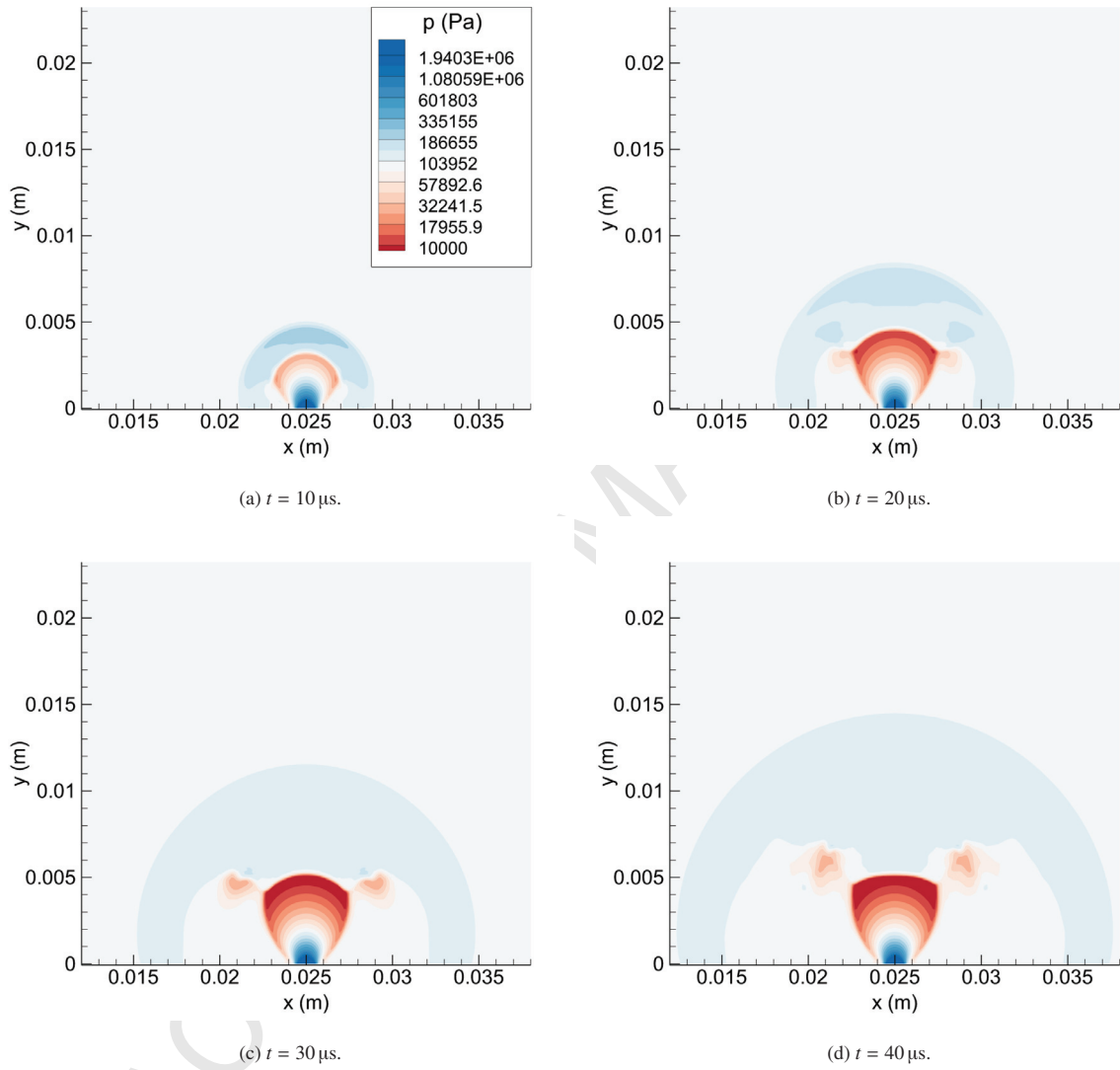


Figure 12: CO₂ jet A: Pressure contours of the developing shock. Plane through $z = 0.025$ m. 400^3 computational cells.

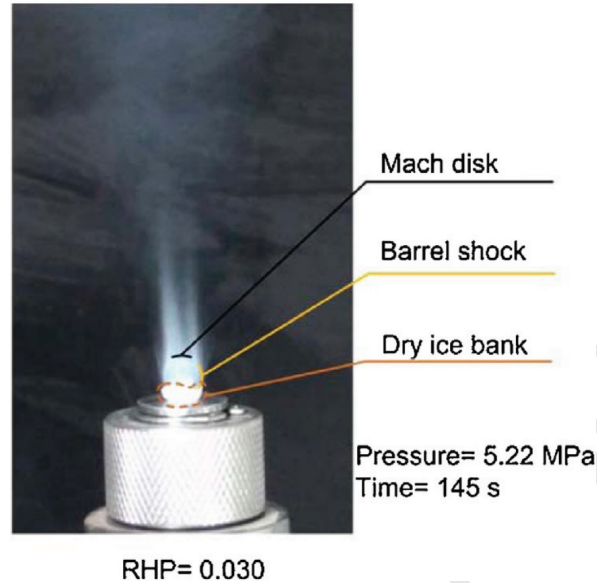


Figure 13: Photograph of CO₂ jet A. Reprinted from Figure 7 in Li *et al.* [42], copyright (2016), with permission from Elsevier.

463 6.2.1. Case description and computational set-up

464 The set-up is analogous to that in Case A, except that the orifice diameter is four times larger. The inlet condition
 465 corresponds to saturated gas. Pure CO₂ of temperature $T = -3.5^\circ\text{C}$ and pressure $p = 31.0$ bar is expanded through
 466 a round hole of diameter $d_e = 4$ mm. The Reynolds number at the inlet is 2×10^6 . The initial temperature in the
 467 computational domain is assumed to be $T_0 = 20^\circ\text{C}$.

468 The computational domain is a cube of edge length 10 cm, divided into an equidistant grid with 200 cells in each
 469 direction.

470 6.2.2. Results

471 Figure 16 shows contours of the absolute velocity plotted at $t = 0.28$ ms. The Mach-disk position is at 16.1 mm
 472 and the width of the structure is 21.7 mm. In this case, the correlation (32) gives $l_{MD} \approx 14.4$ mm for the Mach-disk
 473 position, which is a difference of 12% – somewhat larger than in Case A.

474 The experimental values found by Pursell [44] are 17.8 mm and 21.9 mm, for the Mach-disk position and the
 475 ‘effective diameter’, respectively. Hence, the simulated Mach-disk position lies between that measured by Pursell and
 476 the one given by the correlation. The agreement is very good between the simulated and measured effective diameter.
 477 Further, the barrel-shock structure seen in Figure 16 closely corresponds to the photograph given in Figure 5(b) in
 478 Pursell [44].

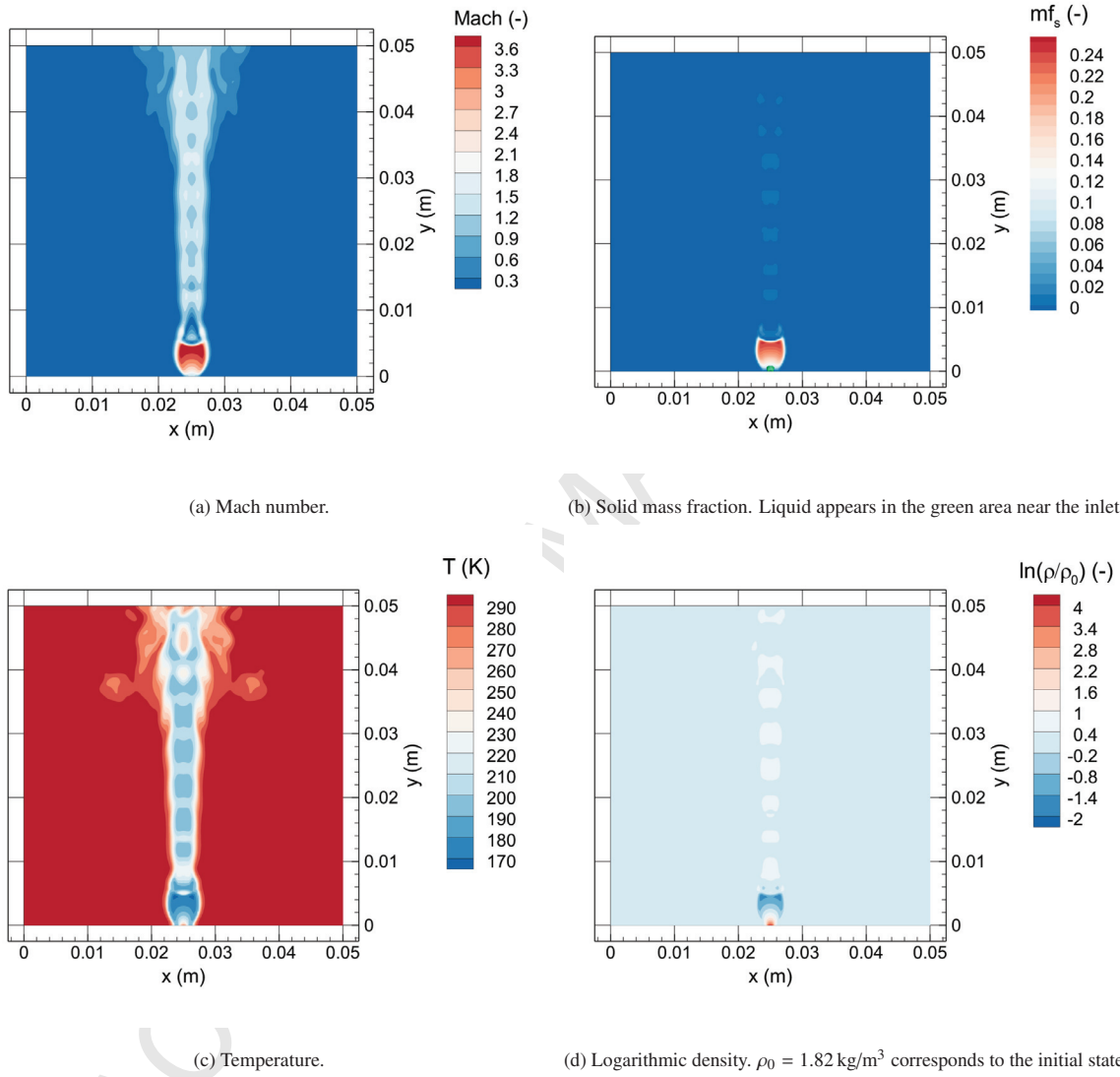


Figure 14: CO₂ jet A: Snapshots at 0.5 ms, where the barrel shock is in a steady state. Plane through $z = 0.025 \text{ m}$. 200^3 computational cells.

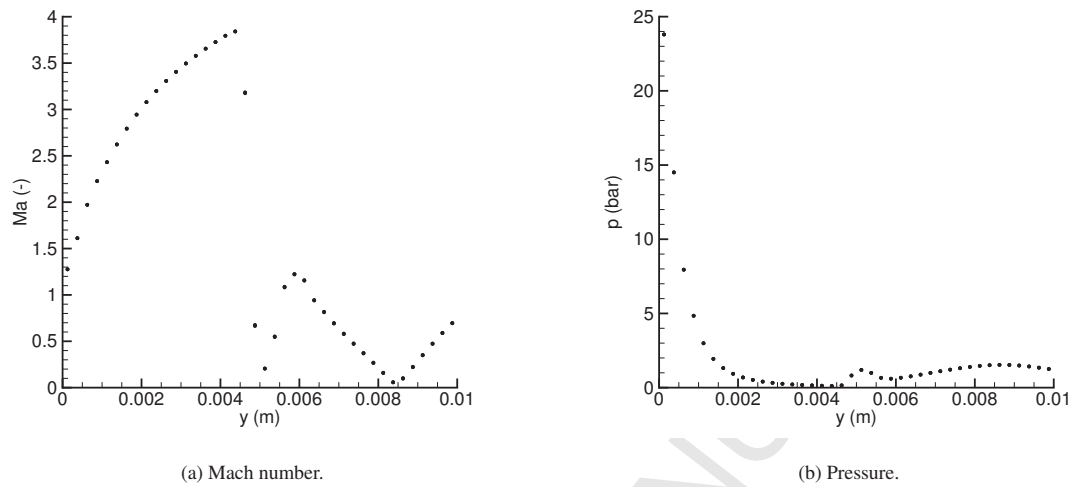


Figure 15: CO₂ jet A: Mach number and pressure plotted along the jet centre line at 0.5 ms.

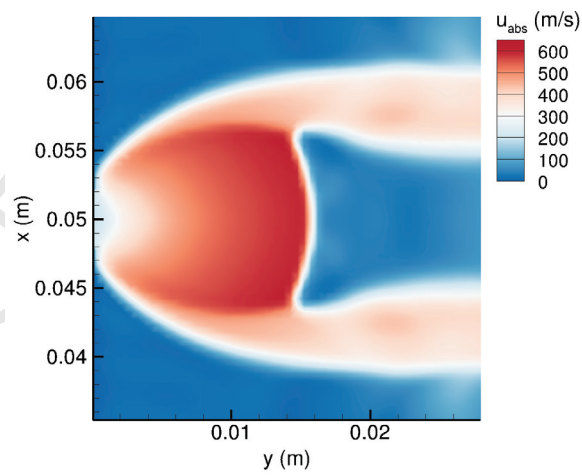


Figure 16: CO₂ jet B: Absolute velocity in a plane through $z = 0.025$ m. Snapshot at $t = 0.28$ ms.

479 7. Conclusions

480 We have developed a high-order finite-volume method capable of handling single-phase, two-phase (gas-liquid)
 481 and three-phase (gas-solid-liquid) flow with discontinuities. The spatial and temporal discretization is similar to that
 482 of Coralic and Colonius [13], employing a fifth-order WENO scheme and a third-order strong-stability-preserving
 483 Runge–Kutta method. In the present case, however, the model formulation is based on the homogeneous equilibrium
 484 model. The fluid phase behaviour is calculated using a suitable EOS and assuming full local thermodynamic equilibrium.
 485 This approach requires special care in the implementation of the flash algorithms required to translate the state variables
 486 into primitive variables.

487 The method has been validated using various benchmark cases, showing robust behaviour and high-order conver-
 488 gence for smooth single- and two-phase flow. Further, the calculation of a turbulent air jet was validated by comparing
 489 with data from Deo *et al.* [41]. Finally, the method was employed to calculate a highly underexpanded CO₂ jet
 490 exhibiting phase transition and three-phase flow. To this end, the Span and Wagner [21] reference EOS was employed.
 491 The method was able to robustly and accurately capture the complex and intertwined thermo- and fluid dynamics. The
 492 shape and dimensions of the barrel shock closely corresponded with the observations of Pursell [44]. The position of
 493 the Mach disk was correctly predicted with reference to the correlation recommended by Franquet *et al.* [43], and good
 494 agreement was obtained with the photograph of Li *et al.* [42].

495 We intend to further develop the method and apply it for the calculation of complex CO₂ flows occurring in jets,
 496 process equipment and pipelines or wells.

497 Acknowledgments

498 This work was carried out in the 3D Multifluid Flow project funded by the Research Council of Norway through
 499 the basic grant to SINTEF Energy Research. Some of the computations were performed thanks to a resource allocation
 500 at the Notur high-performance computing infrastructure (NN9432K).

501 AppendixA. Characteristic decomposition for general EOS

502 Coralic and Colonius [13] perform reconstruction in the local characteristic variables. They calculate these by
 503 multiplying their vector of primitive variables with locally valid transformation matrices. The matrices they give are
 504 valid for the stiffened-gas EOS. Since the ideal-gas EOS is a special case of the stiffened-gas EOS, they are also valid
 505 for ideal gas. Here we present transformation matrices that can be used with a general EOSs.

506 We motivate the procedure for computing the local characteristic variables by first rewriting the system (1) into a
 507 quasi-linear form in terms of a set of variables \mathbf{R} ,

$$\partial_t \mathbf{R} + A \partial_x \mathbf{R} + B \partial_y \mathbf{R} + C \partial_z \mathbf{R} = \mathbf{0}. \quad (\text{A.1})$$

508 Herein, $\mathbf{A} = \partial_{\mathbf{R}}\mathbf{F}$, $\mathbf{B} = \partial_{\mathbf{R}}\mathbf{G}$ and $\mathbf{C} = \partial_{\mathbf{R}}\mathbf{H}$ are the Jacobian matrices. Like Coralic and Colonius [13], we have omitted
 509 the diffusive fluxes and source terms as we are interested in the characteristics of the advective equation system. The
 510 vector \mathbf{R} is

$$\mathbf{R} = [\rho, u_x, u_y, u_z, s]^T, \quad (\text{A.2})$$

511 and the Jacobian matrices are

$$\mathbf{A} = \begin{bmatrix} u_x & \rho & 0 & 0 & 0 \\ \frac{c^2}{\rho} & u_x & 0 & 0 & \frac{1}{\rho} \left(\frac{\partial p}{\partial s} \right)_{\rho} \\ 0 & 0 & u_x & 0 & 0 \\ 0 & 0 & 0 & u_x & 0 \\ 0 & 0 & 0 & 0 & u_x \end{bmatrix}, \quad (\text{A.3})$$

512

$$\mathbf{B} = \begin{bmatrix} u_y & 0 & 0 & 0 & 0 \\ 0 & u_y & 0 & 0 & 0 \\ \frac{c^2}{\rho} & 0 & u_y & 0 & \frac{1}{\rho} \left(\frac{\partial p}{\partial s} \right)_{\rho} \\ 0 & 0 & 0 & u_y & 0 \\ 0 & 0 & 0 & 0 & u_y \end{bmatrix}, \quad (\text{A.4})$$

513 and

$$\mathbf{C} = \begin{bmatrix} u_z & 0 & 0 & 0 & 0 \\ 0 & u_z & 0 & 0 & 0 \\ 0 & 0 & u_z & 0 & 0 \\ \frac{c^2}{\rho} & 0 & 0 & u_z & \frac{1}{\rho} \left(\frac{\partial p}{\partial s} \right)_{\rho} \\ 0 & 0 & 0 & 0 & u_z \end{bmatrix}, \quad (\text{A.5})$$

514 where c is the speed of sound.

515 The equation system (A.1), has one set of characteristic variables for each direction x , y and z . Here we consider
 516 the x -direction only, as the treatment of y and z is analogous. The matrix \mathbf{A} can be written in terms of a diagonal
 517 decomposition,

$$\mathbf{A} = \mathbf{P}\mathbf{\Lambda}\mathbf{P}^{-1} \quad (\text{A.6})$$

518 where $\mathbf{\Lambda}$ is the diagonal matrix of eigenvalues and the columns of \mathbf{P} are the right eigenvectors of \mathbf{A} .

$$\mathbf{\Lambda} = \begin{bmatrix} u_x & 0 & 0 & 0 & 0 \\ 0 & u_x & 0 & 0 & 0 \\ 0 & 0 & u_x & 0 & 0 \\ 0 & 0 & 0 & u_x - c & 0 \\ 0 & 0 & 0 & 0 & u_x + c \end{bmatrix} \quad (\text{A.7})$$

$$\mathbf{P} = \begin{bmatrix} 0 & 0 & -\frac{1}{c^2} \left(\frac{\partial p}{\partial s} \right)_\rho & -\frac{\rho}{c} & \frac{\rho}{c} \\ 0 & 0 & 0 & 1 & 1 \\ 1 & 0 & 0 & 0 & 0 \\ 0 & 1 & 0 & 0 & 0 \\ 0 & 0 & 1 & 0 & 0 \end{bmatrix} \quad (\text{A.8})$$

$$\mathbf{P}^{-1} = \begin{bmatrix} 0 & 0 & 1 & 0 & 0 \\ 0 & 0 & 0 & 1 & 0 \\ 0 & 0 & 0 & 0 & 1 \\ -\frac{c}{2\rho} & \frac{1}{2} & 0 & 0 & -\frac{1}{2\rho c} \left(\frac{\partial p}{\partial s} \right)_\rho \\ \frac{c}{2\rho} & \frac{1}{2} & 0 & 0 & \frac{1}{2\rho c} \left(\frac{\partial p}{\partial s} \right)_\rho \end{bmatrix} \quad (\text{A.9})$$

519 If we now assume that the matrices \mathbf{P} and \mathbf{P}^{-1} are locally frozen in time and space, and thus commute with the
520 differential operators, we can write the x -direction part of (A.1) as

$$\partial_t \mathbf{X} = \Lambda \partial_x \mathbf{X}, \quad (\text{A.10})$$

521 where

$$\mathbf{X} = \mathbf{P}^{-1} \mathbf{R}. \quad (\text{A.11})$$

522 The equation system (A.10) has the form of a decoupled system of advection equations and is locally valid to the
523 extent that the local temporal and spatial variations in \mathbf{R} are small. Thus \mathbf{X} is a local approximation to the characteristic
524 variables for advection in the x -direction.

525 We apply this approximation when performing reconstruction in the local characteristic variables. Before recon-
526 struction to the cell edge quadrature points at $i + 1/2, j, k$, we calculate the characteristic variables in all cells ℓ, m, n in
527 the stencil,

$$\mathbf{X}_{\ell,m,n} = \mathbf{P}_{i+1/2,j,k}^{-1} \mathbf{R}_{\ell,m,n}. \quad (\text{A.12})$$

528 using the same projection matrix $\mathbf{P}_{i+1/2,j,k}^{-1}$. The projection matrix is calculated using a simple arithmetic mean of the
529 fluid state at i, j, k and $i + 1, j, k$.

530 After reconstruction, we have the characteristic variables at the quadrature points on the left and right side of the
531 cell edge $i + 1/2, j, k$. The variables \mathbf{R} at these points are obtained by multiplying with the inverse projection matrix,

$$\mathbf{R}_{i+1/2,j_\ell,k_m}^L = \mathbf{P}_{i+1/2,j,k} \mathbf{X}_{i+1/2,j_\ell,k_m}^L, \quad (\text{A.13})$$

$$\mathbf{R}_{i+1/2,j_\ell,k_m}^R = \mathbf{P}_{i+1/2,j,k} \mathbf{X}_{i+1/2,j_\ell,k_m}^R. \quad (\text{A.14})$$

532 [1] IPCC. *Climate Change 2014: Synthesis Report. Contribution of Working Groups I, II and III to the Fifth Assessment Report of the*
533 *Intergovernmental Panel on Climate Change*. Geneva, Switzerland: IPCC, 2014. URL <http://www.ipcc.ch/report/ar5/syr/>.

- 534 [2] Munkejord ST, Hammer M, Løvseth SW. CO₂ transport: Data and models – A review. *Appl Energy* 2016; 169:499–523.
535 doi:10.1016/j.apenergy.2016.01.100.
- 536 [3] Witlox HWM, Harper M, Oke A, Stene J. Validation of discharge and atmospheric dispersion for unpressurised and pressurised carbon dioxide
537 releases. *Process Saf Environ* 2014; 92(1):3–16. doi:10.1016/j.psep.2013.08.002.
- 538 [4] Woolley RM, Fairweather M, Wareing CJ, Proust C, Hebrard J, Jamois D, Narasimhamurthy VD, Storvik IE, Skjold T, Falle SAEG, Brown S,
539 Mahgerefteh H, Martynov S, Gant SE, Tsangaris DM, Economou IG, Boulougouris GC, Diamantonis NI. An integrated, multi-scale modelling
540 approach for the simulation of multiphase dispersion from accidental CO₂ pipeline releases in realistic terrain. *Int J Greenh Gas Con* 2014;
541 27:221–238. doi:10.1016/j.ijggc.2014.06.001.
- 542 [5] Jamois D, Proust C, Hebrard J. Hardware and instrumentation to investigate massive releases of dense phase CO₂. *Can J Chem Eng* 2015;
543 93(2):234–240. doi:10.1002/cjce.22120.
- 544 [6] Hammer M, Ervik Å, Munkejord ST. Method using a density-energy state function with a reference equation of state for fluid-dynamics
545 simulation of vapor-liquid-solid carbon dioxide. *Ind Eng Chem Res* 2013; 52(29):9965–9978. doi:10.1021/ie303516m.
- 546 [7] Wareing CJ, Woolley RM, Fairweather M, Falle SAEG. A composite equation of state for the modeling of sonic carbon dioxide jets in carbon
547 capture and storage scenarios. *AIChE J* 2013; 59(10):3928–3942. doi:10.1002/aic.14102.
- 548 [8] Wareing CJ, Fairweather M, Falle SAEG, Woolley RM. Validation of a model of gas and dense phase CO₂ jet releases for carbon capture and
549 storage application. *Int J Greenh Gas Con* 2014; 20:254–271. doi:10.1016/j.ijggc.2013.11.012.
- 550 [9] Woolley RM, Fairweather M, Wareing CJ, Falle SAEG, Proust C, Hebrard J, Jamois D. Experimental measurement and Reynolds-
551 averaged Navier–Stokes modelling of the near-field structure of multi-phase SO₂ jet releases. *Int J Greenh Gas Con* 2013; 18:139–149.
552 doi:10.1016/j.ijggc.2013.06.014.
- 553 [10] Falle SAEG. Self-similar jets. *Mon Not R Astron Soc* 1991; 250(3):581–596. doi:10.1093/mnras/250.3.581.
- 554 [11] Titarev VA, Toro EF. Finite-volume WENO schemes for three-dimensional conservation laws. *J Comput Phys* 2004; 201(1):238–260.
555 doi:10.1016/j.jcp.2004.05.015.
- 556 [12] Jiang GS, Shu CW. Efficient implementation of weighted ENO schemes. *J Comput Phys* 1996; 126(1):202–228. doi:10.1006/jcph.1996.0130.
- 557 [13] Coralic V, Colonius T. Finite-volume weno scheme for viscous compressible multicomponent flows. *J Comput Phys* 2014; 274:95–121.
558 doi:10.1016/j.jcp.2014.06.003.
- 559 [14] Balay S, Abhyankar S, Adams MF, Brown J, Brune P, Buschelman K, Dalcin L, Eijkhout V, Groppe WD, Kaushik D, Knepley MG, McInnes
560 LC, Rupp K, Smith BF, Zampini S, Zhang H, Zhang H. PETSc Web page. 2016. URL <http://www.mcs.anl.gov/petsc>.
- 561 [15] Menikoff R, Plohr BJ. The Riemann problem for fluid flow of real materials. *Rev Mod Phys* 1989; 61(1):75–130.
562 doi:10.1103/RevModPhys.61.75.
- 563 [16] Menikoff R. Empirical equations of state for solids. In: Horie Y, editor, *Shock Wave Science and Technology Reference Library*, vol. 2, pp.
564 143–188. Berlin: Springer, 2007; doi:10.1007/978-3-540-68408-4_4.
- 565 [17] Saurel R, Petitpas F, Abgrall R. Modelling phase transition in metastable liquids: application to cavitating and flashing flows. *J Fluid Mech*
566 2008; 607:313–350. doi:10.1017/S0022112008002061.
- 567 [18] Zein A, Hantke M, Warnecke G. Modeling phase transition for compressible two-phase flows applied to metastable liquids. *J Comput Phys*
568 2010; 229(8):2964–2998. doi:10.1016/j.jcp.2009.12.026.
- 569 [19] Rodio MG, Abgrall R. An innovative phase transition modeling for reproducing cavitation through a five-equation model and theoretical
570 generalization to six and seven-equation models. *Int J Heat Mass Tran* 2015; 89:1386–1401. doi:10.1016/j.ijheatmasstransfer.2015.05.008.
- 571 [20] Dumbser M, Iben U, Munz CD. Efficient implementation of high order unstructured WENO schemes for cavitating flows. *Comput Fluids*
572 2013; 86:141–168. doi:10.1016/j.compfluid.2013.07.011.
- 573 [21] Span R, Wagner W. A new equation of state for carbon dioxide covering the fluid region from the triple-point temperature to 1100 K at
574 pressures up to 800 MPa. *J Phys Chem Ref Data* 1996; 25(6):1509–1596. doi:10.1063/1.555991.
- 575 [22] Aursand E, Dumoulin S, Hammer M, Lange HI, Morin A, Munkejord ST, Nordhagen HO. Fracture propagation control in CO₂ pipelines:
576 Validation of a coupled fluid-structure model. *Eng Struct* 2016; 123:192–212. doi:10.1016/j.engstruct.2016.05.012.

- 577 [23] Talemi RH, Brown S, Martynov S, Mahgerefteh H. Hybrid fluid-structure interaction modelling of dynamic brittle fracture in steel pipelines
578 transporting CO₂ streams. *Int J Greenh Gas Con* 2016; 54(2):702–715. doi:10.1016/j.ijggc.2016.08.021.
- 579 [24] Landau LD, Lifshitz EM. *Fluid Mechanics, Course of Theoretical Physics*, vol. 6. 2nd ed. Oxford, UK: Butterworth Heinemann, 1987. ISBN
580 0-7506-2767-0.
- 581 [25] Peng DY, Robinson DB. A new two-constant equation of state. *Ind Eng Chem Fund* 1976; 15(1):59–64. doi:10.1021/i160057a011.
- 582 [26] Ely JF, Hanley HJM. Prediction of transport properties. 1. Viscosity of fluids and mixtures. *Ind Eng Chem Fund* 1981; 20(4):323–332.
583 doi:10.1021/i100004a004.
- 584 [27] Poinso T, Lele SK. Boundary conditions for direct simulations of compressible viscous flow. *J Comput Phys* 1992; 101:104–129.
- 585 [28] Sutherland JC, Kennedy CA. Improved boundary conditions for viscous, reactive, compressible flows. *J Comput Phys* 2003; 191:502–524.
- 586 [29] Toro EF, Billett SJ. Centred TVD schemes for hyperbolic conservation laws. *IMA J Numer Anal* 2000; 20(1):47–79.
587 doi:10.1093/imanum/20.1.47.
- 588 [30] Toro EF. *Riemann solvers and numerical methods for fluid dynamics*. 2nd ed. Berlin: Springer-Verlag, 1999. ISBN 3-540-65966-8.
589 doi:10.1007/b79761.
- 590 [31] Ketcheson DI, Robinson AC. On the practical importance of the SSP property for Runge-Kutta time integrators for some common Godunov-type
591 schemes. *Int J Numer Meth Fl* 2005; 48(3):271–303. doi:10.1002/fld.837.
- 592 [32] Giljarhus KET, Munkejord ST, Skaugen G. Solution of the Span-Wagner equation of state using a density-energy state function for fluid-dynamic
593 simulation of carbon dioxide. *Ind Eng Chem Res* 2012; 51(2):1006–1014. doi:10.1021/ie201748a.
- 594 [33] Henderson LF. General laws for propagation of shock waves through matter. In: Ben-Dor G, Igra O, Elperin T, editors, *Handbook of Shock*
595 *Waves*, vol. 1, chap. 2, pp. 144–183. San Diego, CA, USA: Academic Press, 2000; .
- 596 [34] Toselli A, Widlund OB. *Domain Decomposition Methods — Algorithms and Theory*. Springer Berlin Heidelberg, 2005. ISBN 978-3-540-
597 20696-5. doi:10.1007/b137868.
- 598 [35] Balay S, Gropp WD, McInnes LC, Smith BF. Efficient management of parallelism in object oriented numerical software libraries. In: Arge E,
599 Bruaset AM, Langtangen HP, editors, *Modern Software Tools in Scientific Computing*. Birkhäuser Press, 1997; pp. 163–202.
- 600 [36] Ervik Å, Munkejord ST, Müller B. Extending a serial 3D two-phase CFD code to parallel execution over MPI by using the PETSc
601 library for domain decomposition. In: *CFD2014: The 10th International Conference on Computational Fluid Dynamics In the Oil &*
602 *Gas, Metallurgical and Process Industries*. SINTEF, 2014; URL [http://www.sintef.no/globalassets/project/cfd2014/docs/
603 official_proceedings_cfd2014-redusert-filstr.pdf](http://www.sintef.no/globalassets/project/cfd2014/docs/official_proceedings_cfd2014-redusert-filstr.pdf).
- 604 [37] Balsara DS, Shu CW. Monotonicity preserving weighted essentially non-oscillatory schemes with increasingly high order of accuracy. *J*
605 *Comput Phys* 2000; 160(2):405–452. doi:10.1006/jcph.2000.6443.
- 606 [38] Woodward P, Colella P. The numerical simulation of two-dimensional fluid flow with strong shocks. *J Comput Phys* 1984; 54(1):115–173.
607 doi:10.1016/0021-9991(84)90142-6.
- 608 [39] Kemm F. On the proper setup of the double Mach reflection as a test case for the resolution of gas dynamics codes. *Comput Fluids* 2016;
609 132:72–75. doi:10.1016/j.compfluid.2016.04.008.
- 610 [40] Shi J, Hu C, Shu CW. A technique of treating negative weights in WENO schemes. *J Comput Phys* 2002; 175(1):108–127.
611 doi:10.1006/jcph.2001.6892.
- 612 [41] Deo RC, Nathan GJ, Mi J. Comparison of turbulent jets issuing from rectangular nozzles with and without sidewalls. *Exp Therm Fluid Sci*
613 2007; 32(2):596–606. doi:10.1016/j.expthermflusci.2007.06.009.
- 614 [42] Li K, Zhou X, Tu R, Xie Q, Yi J, Jiang X. An experimental investigation of supercritical CO₂ accidental release from a pressurized pipeline. *J*
615 *Supercrit Fluid* 2016; 107:298–306. doi:10.1016/j.supflu.2015.09.024.
- 616 [43] Franquet E, Perrier V, Gibout S, Bruel P. Free underexpanded jets in a quiescent medium: A review. *Prog Aerosp Sci* 2015; 77:25–53.
617 doi:10.1016/j.paerosci.2015.06.006.
- 618 [44] Pursell M. Experimental investigation of high pressure liquid CO₂ release behaviour. In: *Hazards XXIII – Institution of Chemical Engineers*
619 *Symposium Series*, vol. 158. Southport, UK, 2012; pp. 164–171.

Graphical Abstract

